PHYSICAL SCIENCES

Diffusion power spectra as a window into dynamic materials architecture

Sophia N. Fricke[1]*, Mia Salgado[1], Shira Haber[2]†, Jeremy Demarteau[3], Mutian Hua[4], Ah-Young Song[1,2], Brett A. Helms[2,3], Jeffrey A. Reimer[1,2]

Chemical recycling of commodity and specialty polymers presents a multifaceted challenge for industrial societies. On one hand, macromolecular architectures must be engineered to yield durable products that, on the other hand, rapidly deconstruct to recyclable monomers under pre-determined conditions. Polymer deconstruction is a chemical process that requires deep understanding of molecular reactivity in heterogeneous media, where porous material architectures evolve in both space and time. To build this understanding, we develop herein experimental and analytical methods describing sets of diffusive eigenmodes that exist within time-varying, non-Euclidean boundary conditions, a situation commonly encountered in the reactive deconstruction of polymers where chain fragments splay, alter their local dynamics, and evolve in their confinement of reacting media. Diffusion power spectra, discerned experimentally by NMR, yield polymer and solvent frequency-domain velocity autocorrelation functions that are analyzed in the context of physical models for chemical reactions parameterized with fractal mathematics. The results connect local motion in polymers to chemical reactivity during acidolysis of circular elastomers.

INTRODUCTION

Polymer networks offer customizable material properties for a diverse range of products, primarily durable goods. Their degradation over short timescales is undesirable when products are in use; however, rapid deconstruction in a prescribed medium is desirable when products are recycled at end of life. Understanding local chemical dynamics and reactivity of polymer networks, from molecular to macroscopic scales, emerges as crucial to engineering circularity throughout the succession of generation and regeneration (*1*–*3*). Such an understanding remains elusive, given the multiple time- and lengthscales associated with polymer deconstruction. Polymers are known to be fractal objects with self-similarity in lengthscales ranging from the size of the monomer(s) to the total chain length (*4*–*8*). By definition (*6*, *9*–*11*), fractal objects may be categorized as random or nonrandom spatial or temporal patterns. On the basis of literature knowledge of polymers as archetypal fractals, we reveal herein a connection between objects exhibiting fractal structures in space yet also presenting dynamic processes with fractal kinetics in time, an intriguing link between structure and dynamics (*12*, *13*).

We begin by noting that the departure from Euclidean geometry in nano- and microporous media influences the thermal motion of confined molecules (*14*, *15*). Moreover, the nature of molecular confinement in swollen polymer networks, such as in an elastomer undergoing chemical transformation to monomers, has a profound influence on the motion of trapped molecules because the confinement serves as time-varying boundary conditions for local diffusive motion. In the absence of confinement, molecular motion corresponds to planewave eigenmodes, with momenta states given by $\hbar k$, as the product of the reduced Planck constant and the time-independent wave number. When a molecule experiences confinement, boundary conditions restrict its allowed states due to the requirement of zero probability at the boundaries (*16*). When boundaries exhibit surface roughness and irregularities that may be approximated with fractional dimensionality, the diffusion equation must be solved within the constraints of these complex fractal boundary conditions (*17*–*19*). This approach is necessary to quantify essential and underexplored aspects of polymer deconstruction to reusable monomers.

Small-molecule motion is typically thought of as Brownian, yet the fractal nature of a heterogeneous network boundary (e.g., pore walls) presents nonrandom modes that deviate from a traditional Markovian description (*5*, *20*, *21*). The prolonged memory that arises from confinement influences extended motional coherence and is manifested in the velocity autocorrelation function as an extended time tail (*22*–*25*). This non-Brownian contribution to molecular motion is observable in a diffusion power spectrum, i.e., the spectral density of the velocity autocorrelation function (*26*–*28*). This function is conveniently accessed via diffusion spectra obtained with modulated gradient spin echo (MGSE) trains in nuclear magnetic resonance (NMR) (*29*). Benefits of the MGSE NMR approach include detection of entire sample volumes, versus surfaces as with dynamic light scattering and related approaches (*30*), thereby examining the bulk evolving internal pore structures and connectivity. In particular, the use of low-field, unilateral magnets to accomplish the MGSE NMR measurement enables observation of a wide variety of sample geometries and readily captures the effects of both volume heterogeneity and surface complexity. Moreover, the time- and lengthscales accessed via frequency-filtered MGSE trains readily span frequencies of molecular motion from 0 to 10,000 Hz. Unexpectedly, MGSE NMR has not been widely applied to the evolving dynamics in polymers or nano- and microporous systems, in particular, dynamics that are manifested during polymer deconstruction and chemical recycling processes.

Here, we advance and apply MGSE NMR to understand polymer network deconstruction and provide theoretical validation of this approach consistent with a nonlinear (and non-Markovian) derivation of molecular self-diffusion. Diffusion power spectra obtained

[1]Department of Chemical and Biomolecular Engineering, University of California, Berkeley, Berkeley, CA 94720, USA. [2]Materials Sciences Division, Lawrence Berkeley National Laboratory, Berkeley, CA 94720, USA. [3]The Molecular Foundry, Lawrence Berkeley National Laboratory, Berkeley, CA 94720, USA. [4]School of Environmental and Forest Sciences, University of Washington, Seattle, WA 98195, USA.
*Corresponding author. Email: snfricke@berkeley.edu
†Present address: Department of Chemistry, Ben-Gurion University of the Negev, Beer-Sheva 84105, Israel.

from these experiments are presented as an efficient experimental means of observing molecular dynamics across broad length- and timescales in the complex and evolving media associated with polymer deconstruction. These results clarify the origins of previous findings of an unexpected rate acceleration in polymer network deconstruction via mechanochemical bond activation (*31*). Further, we showcase the ability of MGSE NMR and the associated diffusion spectra to identify the extent of porous network confinement with a high degree of sensitivity and resolution, upon which we elaborate using a series of elastomers that vary in their dynamic materials architectures with respect to both chemical cross-links and degree of entanglement.

RESULTS

The interplay of polymer dynamics, including factors such as chain length, network entanglement, and interactions with surrounding environments, offers a rich landscape for tailoring material transport properties. Figure 1 conceptualizes the approach we take to address this landscape. The inset in Fig. 1A depicts a cross-linked elastomer network undergoing acidolytic transformation, a process mediated by diffusive transport of solvated protons through a heterogeneous medium. From the MGSE NMR pulse sequence shown diagrammatically in Fig. 1B, the exemplary data in Fig. 1C demonstrate that the normalized echo amplitudes decay from diffusive signal attenuation as a function of the number of echoes, N_{echoes}; relaxation does not contribute to this attenuation because all echo trains are recorded with the same fixed total time, T_{total} (further experimental details are provided in Materials and Methods). The decays shown in Fig. 1C can be readily converted to the frequency-dependent diffusion (vide infra). The energy level diagram in Fig. 1D contrasts the density of states available to stiff versus flexible polymer chains (*32*), where increasing polymer flexibility or decreasing entanglement and cross-link density serve to broaden the continuum of energy states available to a polymer system. Such changes could be the result of molecular weight variation, solvation, temperature fluctuations, acidolysis, etc. Correspondingly, the dynamic regimes accessed by a polymer system may be described by a frequency-dependent diffusion spectrum,

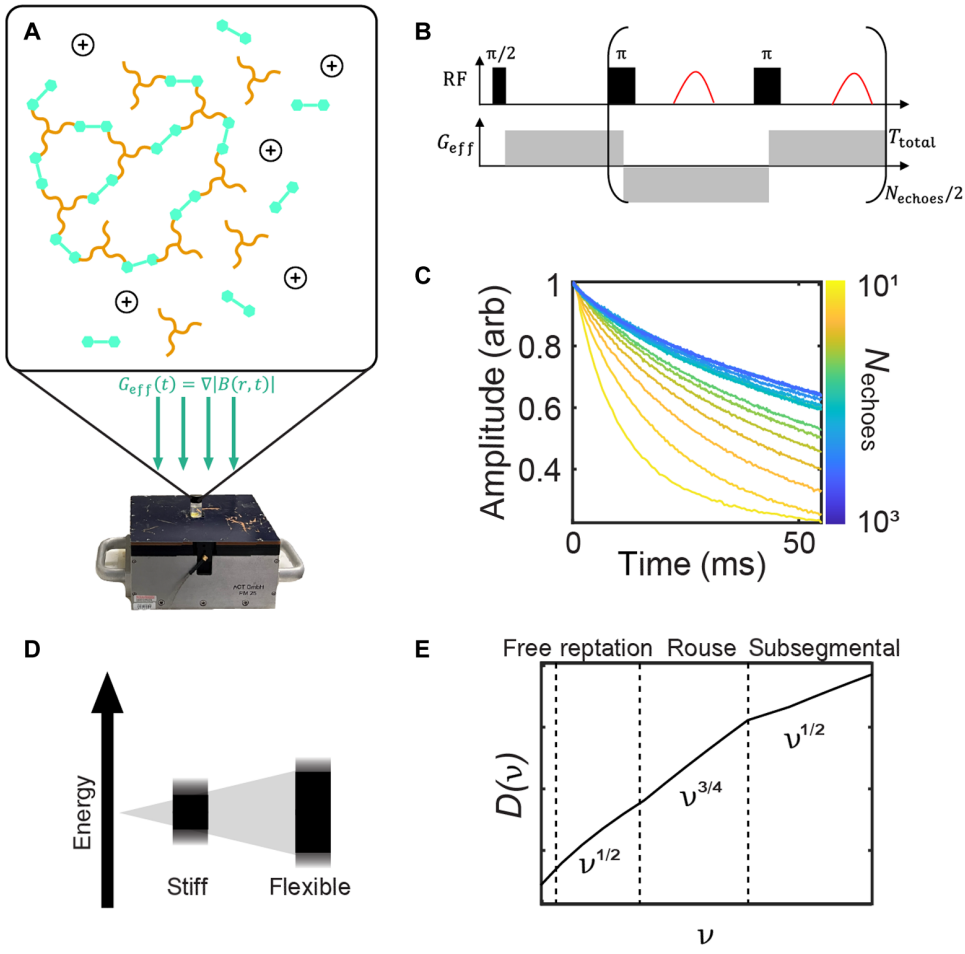

Fig. 1. A graphical depiction of polymer transport, diffusion, and reaction as measured with an MGSE experiment using benchtop NMR. (**A**) shows a polymer sample atop a 0.3-T PM25 NMR-MOUSE unilateral magnet with a static constant gradient of 7 T m^{-1}. (**B**) shows the MGSE pulse sequence that results in a time-varying effective field gradient, G_{eff}, wherein the number of π RF pulses corresponding to the number of echoes, N_{echoes}, in an echo train is varied within a fixed total time, T_{total}. This results in a set of echo time decays as shown in (**C**), with exemplary data for a micellar block copolymer gel made of 50% (w/v) Pluronic F-127 in H_2O. The energy level diagram in (**D**) shows the effect of entanglement on the density of states; entanglement thus affects the dynamic regimes accessed by a polymer system, which are depicted according to the polymer tube model in (**E**).

$D(\nu)$, where the power law scaling from low-to-high frequencies is interpreted as a progression from free diffusion, to reptation, Rouse, and lastly, to subsegmental motion (Fig. 1E) (*33*, *34*).

Reaction kinetics are scale-variant in heterogeneous systems

We consider first the influence of heterogeneity of the polymer surface on the chemical kinetics of polymer decomposition. These reaction kinetics are fundamentally influenced by the scale of a reaction and the surface areas where reactants interact (*35*). At the macroscopic level, the reacting wavefront is observable with operando magnetic resonance imaging (MRI); the changing wavefront with time for large-scale reactions may exhibit behaviors that diverge from classical predictions based solely on consideration of micro- or nanoscale chemistry with homogeneously distributed reactants and products (*36*). In the classically ideal case, increased effective surface areas enhance the frequency of molecular collisions and facilitate more rapid reaction rates. However, discrepancies arise in the translation to macroscopic regimes where reactants must interact across or diffuse through interfaces (*14*–*16*, *22*, *37*, *38*). In addition, surface-area dependencies become crucial when dealing with catalysts or porous materials, as the active sites available for reaction initiation are directly related to the exposed surface (*35*). Understanding the relationship between reaction kinetics, scale variance, and surface area is vital for designing efficient chemical processes and prescribing the necessary reaction conditions to leverage the dynamic interplay between molecular entities across their relevant length and timescales.

Figure 2 illustrates the MRI-observed effect of macroscopic surface area variation on the instantaneous rate coefficient [$k(t)$] for a depolymerization reaction, and the calculated Hurst exponent (h) and corresponding fractal dimension, which is an indicator of the degree of space-filling, or average dimensionality, in the system through surface complexity and volume heterogeneity. Here, we prepared chemically identical cross-linked polydiketoenamine (PDK-T5000) elastomers with cylindrical geometries of 5 mm in height but with diameters ranging from 4 to 8 mm. When deconstructed in the same reaction medium with continuously recorded axial images to allow rate law analysis as described in (*36*), it is evident that the depolymerization rate scales inversely with the sample size, as expected.

However, regimes of sub-, Brownian, and super-diffusion are observed in Fig. 2B, corresponding to $h < 0.5$, $h = 0.5$, and $h > 0.5$, respectively (*21*). A shift from predominantly superdiffusion at early times to subdiffusion at late times represents an initial prevalence of active transport via polymer swelling being gradually replaced by isotropic yet restricted molecular motion. It must be noted that this interpretation reflects a spatial average resulting from all the modes of diffusion present simultaneously within the sample. We submit that the time variation of h may be understood as the rate of reaction deceleration, or the "jerk," a vector quantity that corresponds to the third derivative of the position of the reaction front over time (*39*). Nonzero jerk is the minimum requirement for chaotic behavior in a system, and successive time derivatives (termed snap, crackle, and pop) may be used to linearize the behavior of the chemical wavefront and to model deceleration from the maximum, classically predicted speed (*40*).

To better understand the influence of restricted diffusion on chemical reaction rate, we consider the contributions of different frequencies of molecular motion to the superposed modes of diffusion that are collectively detected by measuring power spectra via MGSE NMR experiments (*27*). In an MGSE experiment, a magnetization grating is selectively increased by varying the number of echo train π pulses within a fixed total time and constant magnetic field gradient (Fig. 1B). This creates a bandpass filter for nuclear spin phase coherences corresponding to molecules within the entire volume of the sample that move at similar frequencies. This is in contrast to the typical pulsed field gradient (PFG) method where a superposition of these contributions is detected. The advantage of varying the number of echoes within a fixed time is that it resolves individual contributions across a frequency spectrum, portending relations between the structure and dynamics of a heterogeneous polymer system. The frequency-dependent diffusion coefficient, $D(\omega)$, is given (*28*) as the transport property associated with the velocity autocorrelation function

$$D(\omega) = \frac{1}{3}\int_0^\infty e^{-i\omega t}\langle v(0)\cdot v(t)\rangle dt \quad (1)$$

where $v(t)$ represents the time-dependent velocity, and the scaling by $\frac{1}{3}$ is a dimensional factor corresponding to the magnetic field gradient. We note that the Green-Kubo relations provide a template to obtain the frequency dependence of any other transport property that is similarly associated with a spatial or temporal autocorrelation function (*41*). This is achieved formulaically by relating a macroscopic transport coefficient to the Fourier transform of a correlation function of a microscopic variable. We now consider three cases that may collectively shed light on deconstructing polymer systems.

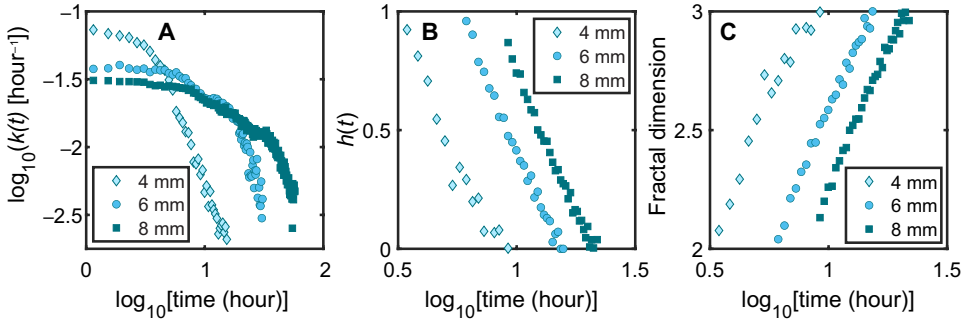

Fig. 2. A demonstration of the scale variance of depolymerization reaction kinetics. The comparative time-dependent rates of PDK-T5000 cylinders of three different diameters deconstructing in 5 M H_2SO_4, as calculated from operando MR images. From the set of time-dependent reaction rates, $k(t)$, in (**A**), the time-dependent Hurst exponents, $h(t)$, and the fractal dimension are calculated in (**B**) and (**C**) as $\frac{\partial k}{\partial t}$ and $3 - h$, respectively (*36*).

Case 1: Water confinement and polymer network architecture

First, we examine $D(\nu)$ when water is present within various swelled elastomer networks, i.e., without the temporal influence of chemical reaction (Fig. 3). We emphasize here that the observed values of $D(\nu)$ for water in polymer matrices are not expected to be lower than the corresponding value for pure water at all frequencies. This is because, first, the recorded signal includes contributions from protons bound to, or in exchange with, the polymer matrices themselves. Second, higher-order harmonics are physically reasonable solutions to the diffusion equation for cavity-confined water. These increased-energy eigenmodes are expected to contribute at higher frequencies, although quantitative prediction is challenging. It is also possible, although unproven here, that the contribution of these modes to traditional PFG NMR experiments may lead to delta (Δ) time dependence in self-diffusion coefficients calculated with the Stejskal-Tanner equation for systems with predominantly restricted diffusion (*27*, *37*, *42*–*45*).

It is evident in Fig. 3A that increased high-frequency modes of diffusion are available to water in confined environments provided by network polymers compared to unrestricted water, dimethylformamide (DMF), and a micellar gel Pluronic F-127. Here, we note that the abundant proton signal from water vis-à-vis the polymer network provides reasonable spectral selectivity to water. The values of $D(\nu)$ for freely diffusing water and DMF are consistent with traditional PSGE-NMR (zero frequency) diffusion coefficients (*25*, *46*, *47*). The remaining samples represent matrices with increasingly hindered motion for controlled comparison to the diffusion spectrum of free water (*47*). Thus, observation of increased water diffusivity at frequencies of 5 to 10 kHz reports on the degree of confinement in surrounding network architecture. The degree of this increase may be conveniently expressed by plotting the scaling power of $D(\nu)$, from which $h(\nu)$ is calculated from an expression for fractional, nonlinear (in time) Brownian motion

$$D(t) = \alpha t^{\alpha-1} D(\infty) \tag{2}$$

where the constant α is twice the Hurst exponent, and the conversion from angular to linear frequencies has been invoked for spectroscopic convention (*5*, *21*, *48*).

By plotting normalized frequency-dependent diffusivities of different systems relative to $D(\nu)$ for DMF (Fig. 3B) and water (Fig. 3C), it is possible to isolate the specific changes in the diffusion power spectra that relate to confinement and the dipolar coupling provided by an organic alkane, respectively. From comparison to the diffusion spectrum for free water in Fig. 3C, it is apparent that most changes in diffusion spectra for systems with some degree of confinement are manifest in the high-frequency regime greater than 5 kHz. The diffusion spectra for simple, bulk liquids tend to high-frequency horizontal asymptotes, observed here below the transition from diffusive to ballistic movement in the terahertz regime (*25*, *29*, *46*, *49*).

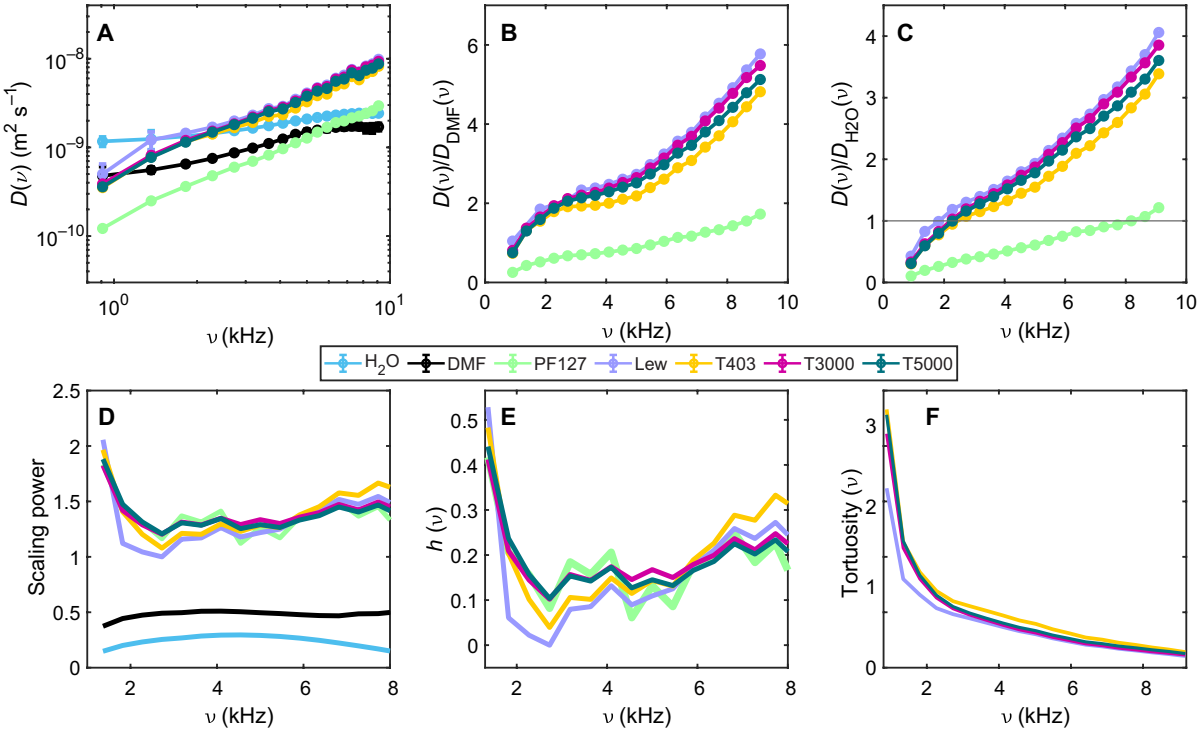

Fig. 3. Diffusion power spectra report the Hurst exponent and tortuosity of water confined in various polymer environments with nonevolving pore structures. (**A**) shows $D(\nu)$ for water confined in a representative selection of polymers: network PDKs of different cross-linking density (PDK-T403, PDK-T3000, and PDK-T5000), and Lewatit VP OC 1065, compared to $D(\nu)$ for an aqueous 50% (w/v) Pluronic F-127 gel, free water, and dimethylformamide (DMF); the latter two as representative simple liquids with unrestricted diffusion. (**B**) shows these $D(\nu)$ spectra relative to the diffusion spectrum of DMF, a representative dipolar-coupled organic liquid without cross-linking. (**C**) shows these spectra relative to the diffusion spectrum of free water, with the horizontal gray line indicating unity. The scaling powers of the diffusion spectra reported in (**D**) connect to the frequency-resolved Hurst exponents, $h(\nu)$, in (**E**). The frequency-resolved tortuosity of the confined water in these various environments, calculated as the inverse of the data reported in (C), is shown in (**F**).

From the diffusion spectra scaling powers shown in Fig. 3D, it is possible to calculate the frequency dependence of the Hurst exponents, $h(\nu)$, as described and simulated in (*21*), and the frequency-dependent tortuosity of confined water as the ratio of their diffusion spectra (Fig. 3, E and F, respectively) (*50*). Notably, water confined in the smallest network polymer, PDK-T403 (plotted in gold), presents the largest h at high frequencies (6 to 8 kHz), followed by water confined in the polymeric anion exchange resin, Lewatit VP OC 1065, an off-the-shelf control sample with uniform nanopore structure (*51*) (plotted in purple). In contrast, these two systems have the smallest values of h at low frequencies from approximately 2 to 4 kHz. Together, these trends appear to result from a higher degree of entanglement and therefore tighter confinement of water in the PDK and Lewatit systems, which manifests in enhanced high-frequency correlated aqueous motion, and suppressed low-frequency, long-range translational motion.

One of the most straightforward critical parameters used to understand transport in porous media is tortuosity, which is most simply understood as the ratio between a curved path and the distance between its two ends (*52*). This arc-chord ratio is 1 for a linear path, $\pi/2$ for a half-circle trajectory, and divergent to infinity for a circular path (*53*–*55*). Intriguingly, this elementary definition of tortuosity intuitively suggests a time and frequency dependence, which also follows from the Green-Kubo derivations of transport properties and time-dependent diffusion as defined here in Eq. 2 (*28*, *56*, *57*). In support of this hypothesis, it was realized that in many typical cases of confined diffusion, the curvature often changes in time. Thus, it was proposed in this case to find a local metric of tortuosity as the spatial derivative of the logarithm of the curvature (*54*). Alternatively, the tortuosity has been estimated as the time integral of the square modulus of the curvature normalized by the chord length (*58*). Tortuosity is therefore closely related to the fractal dimension of the path of a moving particle. Figure 3F demonstrates a local metric of tortuosity that directly follows from the ratio of diffusion spectra for free to confined water, where we see the greatest contribution at low frequencies, where bulk diffusion of water is most changed as a result of confinement (*50*). For the three swelled PDK polymers we consider here, we observe the highest tortuosity for water confined in the smallest network, PDK-T403. The relatively lower values of tortuosity for the Lewatit and water system most likely reflect the averaged contribution of some unconfined water to the measurement.

Next, we immerse the same series of elastomer networks in D_2O to selectively study the slower modes of motion of the polymer chains themselves. As illustrated in Fig. 4A, the increase in diffusivity of polymer protons appears to correspond to increasing network size (i.e., cross-linker molecular weight) from the micellar gel Pluronic F-127, to PDK-T403, to Lewatit VP OC 1065, to PDK-T3000 and PDK-T5000, which are statistically indistinguishable in this regard. Moreover, increased diffusivity probed at frequencies of 5 to 10 kHz or more indicates detection of higher-order vibrational modes of polymer stretching, which may be described by Rouse and Zimm

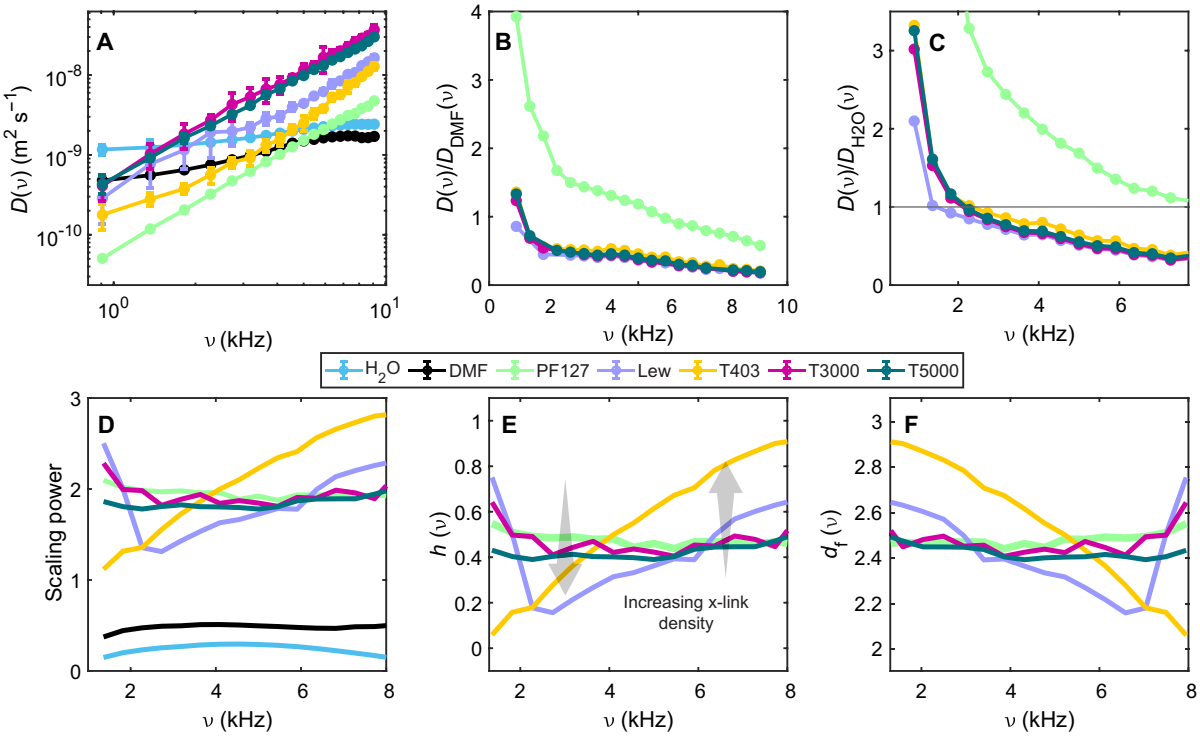

Fig. 4. Diffusion power spectra yield the Hurst exponent and fractal dimension of polymer motional modes with nonevolving pore structures. (**A**) reports $D(\nu)$ for a representative selection of polymers swelled with D_2O: network PDKs of three cross-link densities (PDK-T403, PDK-T3000, and PDK-T5000) and Lewatit VP OC 1065, compared to $D(\nu)$ of a deuterated aqueous 50% (w/v) Pluronic F-127 gel, as well as free water and DMF as representative simple liquids with unrestricted diffusion. (**B**) shows these spectra relative to the diffusion spectrum of DMF, a representative dipolar-coupled alkane system without cross-linking. (**C**) shows these spectra relative to the diffusion spectrum of freely diffusing water, with the horizontal gray line indicating unity. The scaling powers of the diffusion spectra reported in (**D**) relate to the frequency-resolved Hurst exponents, $h(\nu)$ in (**E**), which in turn relate to the frequency-resolved fractal dimension, $d_f(\nu)$, of each system shown in (**F**).

models of polymer dynamics (*8*, *33*), conceptually illustrated in Fig. 1E, and quantified via calculation and analysis of $h(\nu)$.

Analysis of normalized frequency-dependent diffusivities of different systems relative to $D(\nu)$ for DMF (Fig. 4B) and water (Fig. 4C) highlights explicit changes in the diffusion power spectra due to the dipolar coupling provided by an organic alkane and free diffusion of unconfined water, respectively. From comparison to the diffusion spectrum for free water in Fig. 4C, it is apparent that while low-frequency modes of diffusion are attenuated relative to water, high-frequency modes of diffusion are most amplified for systems with low cross-link density. This is indicated by crossing below a ratio of unity; this threshold is marked in Fig. 4C with a horizontal gray line. This corresponds to the frequency range of molecular motions commonly attributed to vibrational dynamics (*8*). One possible interpretation of this result is that the lower–molecular weight network polymers may be too tightly entangled to develop higher modes of vibration, whereas higher–molecular weight network polymers with relatively lower cross-link density may support a higher harmonic range of vibrational movement.

From the diffusion spectra scaling powers shown in Fig. 4D, it is possible to calculate (*21*) the frequency dependence of the Hurst exponents, $h(\nu)$, and the corresponding fractal dimension, $d_f(\nu)$ as $3 - h(\nu)$ (Fig. 4, E and F, respectively). Notably, the lowest–molecular weight network polymer, PDK-T403 (plotted in gold), presents the largest h at high frequencies (6 to 8 kHz), followed by Lewatit VP OC 1065 (plotted in purple). In contrast, these two systems have the smallest values of h at low frequencies from approximately 2 to 4 kHz. The small values of h below 2 kHz may result from differences in the overlap between free diffusion and reptation-type movement of Lewatit VP OC 1065, an anion-exchange resin, and PDK elastomers. Both the high- and low-frequency behaviors of PDK-T403 and Lewatit VP OC 1065 appear to result from a higher degree of entanglement in these systems, which manifests in enhanced high-frequency vibrational motion, and suppressed low-frequency, long-range translational motion (most apparent for PDK-T403), consistent with the results shown in Fig. 3. These two smallest-network materials show the greatest frequency dispersion in fractal dimension, as reported in Fig. 4F. Here, the higher dimensionality [approaching three dimensions (3D)] at low frequencies and lower dimensionality (approaching 2D) at high frequencies suggests the presence of distinct regimes that are clearly separated in high–cross-link density materials. On the other hand, the lower–cross-link density materials considered here reflect apparently frequency-independent average dimensionality of 2.5, perhaps suggesting that the pore spaces are too large and flexible to support distinct regimes that result from cross-linking and entanglement. Together, these observations are consistent with the results of previous studies that suggest one effect of cross-linking is to lock a polymer network into a nonequilibrium state as compared to the same network before the introduction of cross-links (*59*, *60*). By extension, it may be surmised that networks with higher cross-link density will occupy states farther from equilibrium than those with low cross-link density, which manifests as more extreme scaling behavior (*61*, *62*).

To summarize, the primary information we have extracted from diffusion spectra has been obtained via either (i) the scaling power of individual diffusion spectra or (ii) the ratios of diffusion spectra, where one of these $D(\nu)$ spectra has known properties (such as free liquid). The complementary analyses must be interpreted with the recognition that all the superposed modes of detected polymer displacements in Fig. 4 correspond to different translational mechanisms of motion that are simultaneously present in the various systems. These translational modes are in fact eigenmodes of the relevant diffusion equation. The possibility for higher harmonics to serve as solutions to this equation means that it is theoretically feasible for these modes to be detected. Progression to higher frequencies typically corresponds with a crossover from reptation to Rouse-type motion, to subsegmental motion, where the smaller displacements are represented at higher frequencies (*63*). However, the instrumental limitations of measuring solid-state samples on a unilateral, low-field magnet means that some of the fastest relaxing, dipole-coupled protons associated with the polymer backbone will not be detected in this setup. These protons would be the most likely representatives of minimum mean squared displacements, yet they may contribute only minimally to the superposition state, total diffusion spectrum that is recorded.

Case 2: Time-resolved diffusion power spectra

Next, we examine time-resolved MGSE NMR $D(\nu)$ in operando during polymer deconstruction for PDK-T403 in HBr, HCl, and H_2SO_4. The acids, respectively, donate chaotropic, order-neutral, and kosmotropic anions to the reaction medium, modulating the water solvation shells and thereby varying the effective surface areas and pore volumes available for reaction (Fig. 5). Calculation of $h(\nu)$ from $D(\nu)$ allows estimation of the time- and frequency-resolved rate coefficients, $k(\nu, t)$, as

$$k(\nu, t) = k(0)t^{-h(\nu)} \tag{3}$$

This formula has been applied previously to develop rate laws with noninteger molecularity and time-dependent rate coefficients (*13*, *36*) and uses a power law framework that has been well established in other areas of fractal mathematics (*6*, *9*, *10*, *18*, *64*).

Numerical integration of the Hurst exponent yields a prediction of frequency- and time-dependent kinetic rate coefficients, provided that the reaction studied proceeds in the slow, diffusion-mediated limit. Observation of the system in this limit allows the assumption that the kinetic and thermodynamic effects governing the process are operative on analogous timescales. An analytical expression can be developed via Laplace transformation of the Eq. 3, yielding the solution for k in terms of the Laplace frequency, s, as a product of a power law and a gamma function

$$k(s) \cong s^{h-1}\Gamma(1-h) \tag{4}$$

Figure 5 presents data from the deconstructing PDK-T5000 cylinders shown as the diffusion power spectra, Hurst exponents, and derived $k(\nu, t)$ from fastest (HBr; green panel backdrop) to slowest (H_2SO_4; red panel backdrop). There is a trend of decreasing high-frequency modes of diffusion as the reaction progresses from 0 (pale blue) to 48 hours (dark blue), by which time even the slowest deconstructing system in H_2SO_4 had achieved complete depolymerization. This trend is consistent with the hypothesis that cross-link density diminishes as the polymer network breaks apart, which serves to decrease the network confinement of trapped water. We note that the decreased diffusive attenuation with frequency (i.e., higher values of $D(\nu)$ in Fig. 5, A to C) arises from enhanced spin coherence as evidenced by diffusion power spectra with frequency scaling exponents greater than Rouse-type $\propto \nu^{3/4}$. In the early stages of reaction, this trend is indicative of non-Brownian movement of confined water.

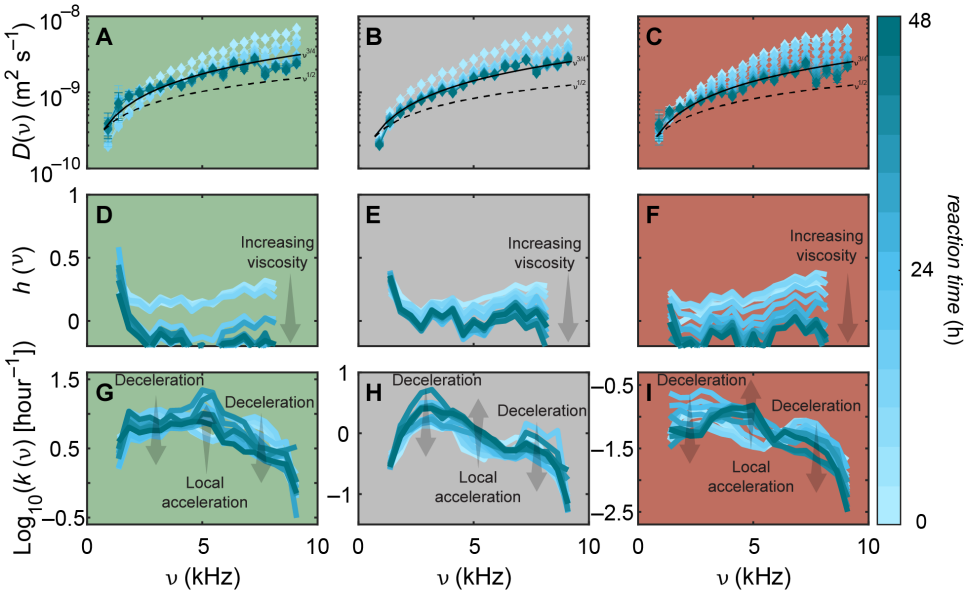

Fig. 5. Time-resolved diffusion power spectra enable operando observation of local depolymerization reaction rates. Overlaid diffusion power spectra for deconstructing PDK-T5000 cylinders 6 mm in diameter and 5 mm in height in 5 M HBr, HCl, and H_2SO_4 (**A** to **C**) yield time- and frequency-resolved Hurst exponents (**D** to **F**), which predict rate coefficients (**G** to **I**). From numerically integrating $h(\nu, t)$ with respect to time, as plotted in [(D) to (F)] and calculated from [(A) to (C)], it is possible to determine as shown in (**G** to **I**) $k(\nu, t)$. As the fastest-depolymerizing system considered here, the PDK-T5000 reacting in HBr (green backdrop; left column) reaches completion of reaction first, which is clear in (D) as the sudden drop in $h(\nu, t)$ at 24 hours toward zero mean. The slowest-depolymerizing system here is PDK-T5000 reacting in H_2SO_4, plotted with a red backdrop in the rightmost column. PDK-T5000 deconstructing in HCl presents a reaction of intermediate rate, plotted with gray backdrop in the center column. h, hours.

As depolymerization progresses and the network breaks apart, the water and released monomer molecules become less correlated in their movement until free tumbling and rotation in solution dominate molecular motion (*65*). As the aqueous reaction medium gains concentration of released monomer, the free tumbling of aqueous molecules becomes more hindered, resulting in increased viscosity and a corresponding decrease in the Hurst exponent as reaction time progresses, shown in Fig. 5, D to F. Whereas there is not a hugely discernible change in rate coefficient over time for the fastest-deconstructing system shown in Fig. 5G, as the reaction medium becomes more kosmotropic (Fig. 5, H and I), the rate coefficient shows a marked decrease over time for the low- and high-frequency regions (~0 to 3 kHz and 6 to 8 kHz), as predicted from the ensemble averages measured via MRI in Fig. 2 and (*36*). Unexpectedly, there is a notable increase in rate coefficient circa 5 kHz apparent in the HBr deconstruction, which likely also manifests in the H_2SO_4 medium. Here, we surmise that the correlation time for molecular motion matches a characteristic timescale for the microscopic reaction mechanism, leading to local acceleration (vide infra). These intriguing observations are contextualized by and are consistent with previous, multiscale investigations of these systems with a variety of experimental techniques (*31*, *36*, *65*). Nonetheless, these findings portend further study to engineer the deconstruction properties of polymer materials based on mapping local acceleration dynamics to specific molecular moieties.

Case 3: Bridging kinetics and thermodynamics in heterogeneous processes

We submit that the frequency dispersion of the time-dependent depolymerization rate coefficients provides additional insight to the instantaneously calculated set of $k(t)$ reported in Fig. 2. From the set of $k(\nu, t)$ shown in Fig. 5 (G to I), it is possible to calculate frequency-dependent order parameters, $F(\nu)$, as the ratio of the initial to final $k(\nu, t)$ via the proportion

$$F(\nu) = \frac{k(\nu, 0)}{k\left(\nu, t_{\text{final}}\right)} \tag{5}$$

as demonstrated in Fig. 6A (*13*, *66*, *67*). From this analysis, it becomes possible to attribute chemical kinetics in regions of relatively faster or slower reaction (i.e., temporally distinct behavior) to specific modes of diffusive behavior in space. These corresponding modes of diffusion can be understood to indicate regions of greater network confinement when their amplitudes over a given set of frequencies differs substantially from that of free water (which displays no effects of confinement and minimal effects of shear viscosity) and DMF (with intramolecular dipolar coupling, but no cross-linking or porous network confinement). Here, we note again the apparent acceleration of order parameter at 5 kHz in the HBr and H_2SO_4 media.

We sum the individual frequency contributions that are spectrally resolved in Fig. 6A to yield a macroscopic order parameter (*13*, *36*, *67*–*69*) (Fig. 6B). We note that we have not performed any normalization based on the number of frequencies sampled. The trend of increasing F with variation of chaotropic-to-kosmotropic reaction media qualitatively reflects the magnitude of changes in self-ordering that are necessary for the system for achieve thermodynamic equilibrium as the low-energy state associated with reaction completion. The most kosmotropic system considered here, H_2SO_4 (shown in red), begins in the most ordered state with the largest solvation shells, and therefore must undergo the greatest amount of change in terms of structural reorganization to achieve uniformly mixed products. This process is diffusion-mediated and entropically driven. On the other

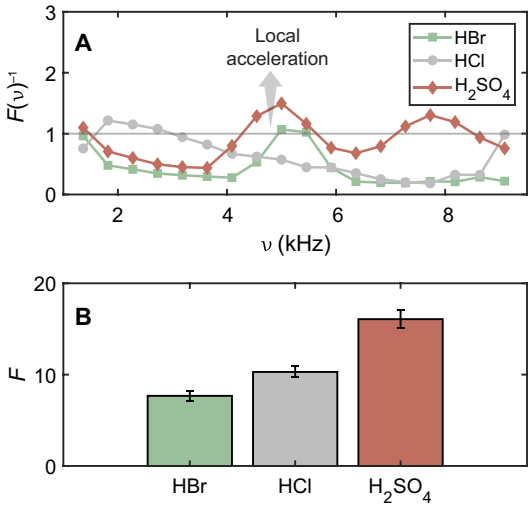

Fig. 6. Frequency dispersion of reaction order parameters. (**A**) compares the frequency-dependent order parameters for PDK-T5000 depolymerization in 5 M HBr, HCl, and H_2SO_4, calculated from the ratio of the initial to final $k(\nu, t)$ plotted in Fig. 5 (G to I). Here, the inverse order parameter is plotted to intuitively show the regions of anomalous local reaction acceleration as $F(\nu)^{-1} > 1$, in contrast to the regions of deceleration with local values of $F(\nu)^{-1} < 1$. The ratio of constant rate is indicated by the horizontal gray line $F(\nu)^{-1} = F(\nu) = 1$. By summing all the individual frequency contributions to $F(\nu)$, it is possible to calculate a macroscopic order parameter, F, independent of frequency, to contrast the differing reaction systems in (**B**).

hand, the most chaotropic system, HBr (shown in green), begins in a randomized state that is closest to thermodynamic equilibrium, and thus presents the smallest order parameter. The reported trend in order parameter increasing together with kosmotropicity of the acid anion, a thermodynamic metric, is consistent with the observed trend in kinetic reaction rate coefficients (*31*, *36*). The correspondence between thermodynamic and kinetic factors is noteworthy and may play a role in the molecular dynamics of other systems.

DISCUSSION

Efficient characterization strategies that illuminate both the structures and dynamics of polymers during chemical transformations are urgently needed for improving the present understanding of polymer deconstruction. Such strategies are presumed to facilitate optimization and tuning of polymer properties that influence circular manufacturing processes. In macroscopically heterogeneous environments such as deconstructing elastomer networks, however, the present literature does not provide insight into the coupling of transport and dynamics to the molecular motion of the reactive medium confined within these networks. As a result, current treatments of molecular dynamics in polymer systems often fall short in capturing the complexity of transport processes, particularly those exhibiting time-variant, non-Euclidean boundary conditions. To bridge this gap, observation of frequency-dependent diffusion is powerful because it offers a direct link between structure and dynamics across time- and lengthscales and can be made sensitive to both an aqueous medium and a polymer network as shown herein.

The MGSE NMR–based method for characterizing the frequency-dependent diffusion of the various molecular moieties present in reactive elastomer networks swelled in aqueous media is shown in the context of physical models parameterized with fractal mathematics. Here, diffusion power spectra connect the microscopic, structural origins of differences of motion to the macroscopic deconstruction rates and bulk-scale depolymerization outcomes. Thus, the NMR-based MGSE method for measuring diffusion power spectra presents a promising avenue for addressing the need for improved characterization strategies for to a circular plastics economy, offering a wealth of chemical and mechanical information from a simple measurement that can be performed with readily customized benchtop NMR systems for operando studies.

The MGSE methods are not without some limitations. Because of the use of a constant magnetic field gradient, the echo time is the parameter varied via changing the number of echoes, rather than gradient strength, for this implementation of MGSE experiments (*70*, *71*). To minimize the effect of relaxation, the total pulse sequence time T_{total} is held constant, here at 55 ms. Thus, the minimum and maximum echo times are the limiting instrumental and physical factors. The minimum here is 50 μs, but is practically limited by only duty cycle. In principle, if the echo time were reduced by a factor of 10 or more, it could be possible to access the hundreds of kilohertz regime of molecular motion, if the effects of convection in aqueous samples could be mitigated. Hardware improvements could realistically enable echo times of 2 to 4 μs with technology that is currently available, and the effects of convection are typically mitigated via temperature control or the reduction of liquid sample volume. On the other hand, the maximum echo time here of 1.1 ms was determined by spin relaxation during this time window, which is accentuated due to the inhomogeneous broadening caused by the unilateral magnet. In a homogeneous field with pulsed magnetic field gradients, this echo time can easily be much longer; however, the minimum echo time would also be much longer, due to the added switching/ramp times for the gradient pulses.

Beyond calibration of the constant magnetic field gradient for calculation, we posit that normalization of diffusion power spectra via control samples is not valid in the same way that it is for PFG experiments that use calibration to a standard, zero frequency value. While such calibrations can potentially provide a prediction of the y intercept in a diffusion spectrum, the shape of the spectrum at nonzero frequencies is determined by a Lorentzian expression from the solution to the diffusion equation (*22*). This full solution accounts for not only zero frequency, or infinite time, translational motion, but also higher-order vibrational movements determined by the density of states, the number of degrees of freedom available to a system, and thus its cross-link density and degree of entanglement as shown in Fig. 1D. In addition, correlated modes of mutual diffusion and non-Brownian motion may contribute to the nonzero frequency part of the diffusion spectrum, thus mandating the use of an expression for mean squared displacement that can account for time dependence with fractionally scaled power laws.

In summary, we demonstrate insights into polymer deconstruction that are not available from traditional methods. Our findings underscore the potential of coupling experimental MGSE measurements of diffusion power spectra with physical models parameterized with fractal mathematics, thereby enhancing both fundamental understanding of polymer motion and kinetics in polymers and providing modeling tools for engineering materials with tailored properties and behaviors. We anticipate that these experimental and analytical tools may serve to advance industrial recycling practices in plastics circularity.

MATERIALS AND METHODS

Experimental design

PDK elastomers were prepared by mixing solutions of triketone monomer and tribranched amine-terminated polypropylene glycol cross-linkers T403, T3000, and T5000 (Huntsman), whose molar masses are nominally 403, 3000, and 5000 g mol^{-1}, respectively (*31*). A thorough description is provided in the Supplementary Materials. For swelling measurements, samples were immersed in an excess of H_2O or D_2O for a minimum of 1 week, to ensure that equilibrium had been achieved before measurement. Acids were prepared in 5 M concentration of HBr, HCl, and H_2SO_4 with chemicals that were obtained from Sigma-Aldrich and used as received. Lewatit VP OC 1065 was purchased from Sigma-Aldrich; the network molecules were evacuated before introduction of H_2O or D_2O. Pluronic F-127 powder was purchased from Sigma-Aldrich; hydrogels were prepared at concentrations of 50% (w/v) with H_2O and D_2O by cooling below 10°C to dissolve the powder, then heating above 10°C to set the gel. Cooling and heating cycles were repeated 15 to 20 times over the course of 12 hours until gels had achieved structural uniformity with no bubbles evident, appeared visually transparent, and irradiation with a collimated infrared laser beam did not result in scattered light.

NMR MGSE (*27*, *29*) measurements were performed at room temperature with an NMR-MOUSE (Mobile Universal Surface Explorer) PM25 0.3-T unilateral magnet (*72*, *73*) and a Magritek Kea II spectrometer at a ^{1}H resonant frequency of 13.11 MHz and a constant magnetic field gradient of 7 T m^{-1}. The number of π radio frequency (rf) pulses in a Carr-Purcell-Meiboom-Gill pulse sequence (CPMG) (*74*, *75*) was varied within a fixed total time to selectively detect the diffusive contribution to signal relaxation and not transverse relaxation, using Prospa version 3.61 software from Magritek (Malvern, PA.). For all experiments, π/2 rf pulse lengths were 2.5 μs, the delay between π rf pulses was varied between 55 and 1100 μs in 20 incremental steps, and the repetition time for signal averaging was 2.4 s to sum either 128 or 4096 CPMG transient signals for the H_2O- and D_2O-based set of samples, respectively. To cancel artifacts arising from pulse imperfections, the initial π/2 rf pulse and the receiver were cycled between $+x$ and $-x$ phase while holding the π rf pulse phase constant at $+y$.

Imaging experiments were carried out with a Pure Devices 0.55-T Magspec magnet interfaced to Drive-L RF-100 and Gradient-600 amplifiers and an actively damped Q probe (Pure Devices GmbH, Germany), at a ^{1}H resonant frequency of 24.36 MHz, and temperature controlled at 29°C. Images were acquired using a standard spin echo pulse sequence (*76*) with an echo time of 5 ms and a repetition time of $5T_1 = 1$ s for the 5 M strong acids, to maximize signal from the aqueous acid and minimize signal from solid PDK with R_2 weighting. A 10-mm square field of view was chosen, corresponding to a 64 by 64 sampling grid with a slice thickness of 5 mm for axial images centered on polymer cylinders 6 mm in height and 8 mm in diameter placed in approximately 1 cc of acid. Zero-filling interpolated the square pixel resolution from 156.2 to 39.1 μm.

Statistical analysis

All simulations and data analysis were accomplished with MatLab (Mathworks, Natick, MA). The calculation of $D(\omega)$ from MGSE experiments was performed using a formula for echo attenuation as a function of gradient modulation frequency,

$$E(\tau, \omega_m) = \sum_i E_{0,i} e^{-\frac{\tau}{T_{2i}} - \frac{8\gamma^2 G^2}{\pi^2 \omega_m^2} D_{zz,i}(\omega_m)\tau} \quad (6)$$

as previously derived via average Hamiltonian theory using a cumulant expansion to second order (*27*, *29*, *77*). Here, $E_{0,i}$ is the initial intensity of the echo train corresponding to the ith component of the signal with transverse relaxation T_{2i}. The strength of the magnetic field gradient is denoted by G, γ is the magnetogyric ratio of the detected nucleus, and $D_{zz,i}(\omega_m)$ refers to the frequency-dependent diffusion coefficient, or the velocity autocorrelation spectrum, of the ith component of the signal along the direction of the magnetic field gradient, which is here denoted as z. The variable τ is the product of the number of spin echoes and the period of π-rf pulses, i.e., twice the echo time, and the modulation frequency, ω_m, is the product of π and the inverse modulation period (*26*, *27*, *29*, *78*).

In MGSE experiments recorded with the static magnetic field gradient of a unilateral magnet, variation of echo time leads to variable π-rf pulse frequency (*70*). As the echo time is increased, R_2 weighting is also increased, as longer echo times allow fast-relaxing signal components to decay between the pulses. This is an unavoidable part of the MGSE experiment; however, by keeping the total time fixed, we have attempted to minimize to some extent the degree of R_2 weighting that occurs. Undoubtedly, the detected signal, and thus, the velocity autocorrelation function, contains contributions from many different groups of protons. This effect is even more compounded by the presence of various dynamic processes across the systems we consider, such as polymer chain motion, chemical exchange, etc. Therefore, the measured velocity autocorrelation functions are best understood as ensemble averages over all the protons in the system.

Measurements were collected in triplicate and error bars represent the statistical mean and SD. Further mathematical derivation is provided in the Supplementary Materials.

Supplementary Materials

This PDF file includes:

Supplementary Text

REFERENCES AND NOTES

1. Ellen MacArthur Foundation, "The New Plastics Economy – Rethinking the Future of Plastics" (2016); https://www.ellenmacarthurfoundation.org/the-new-plastics-economy-rethinking-the-future-of-plastics.
2. Ellen MacArthur Foundation, "The New Plastics Economy – Catalysing Action" (2017); https://www.ellenmacarthurfoundation.org/the-new-plastics-economy-catalysing-action.
3. Ellen MacArthur Foundation, "The Global Commitment 2020 Progress Report" (2019); https://www.ellenmacarthurfoundation.org/news/global-commitment-2020-progress-report-published.
4. B. Mandelbrot, How long is the Coast of Britain? Statistical self-similarity and fractional dimension. *Science* **156**, 636–638 (1967).
5. B. B. Mandelbrot, J. W. Van Ness, Fractional brownian motions, fractional noises and applications. *SIAM Rev.* **10**, 422–437 (1968).
6. A. Bunde, S. Havlin, Eds., *Fractals and Disordered Systems* (Springer Berlin Heidelberg, Berlin, Heidelberg, 1996).
7. J. R. Banavar, M. Lipsicas, J. F. Willemsen, Determination of the random-walk dimension of fractals by means of NMR. *Phys. Rev. B* **32**, 6066 (1985).
8. M. Doi, S. F. Edwards, *The Theory of Polymer Dynamics* (the Clarendon Press, Oxford University Press, New York, 1986).
9. B. B. Mandelbrot, Self-affine fractals and fractal dimension. *Phys. Scr.* **32**, 257–260 (1985).
10. K. Falconer, *Fractal Geometry* (John Wiley & Sons, Ltd, Chichester, UK, 2003).
11. M. Frame, A. Urry, *Fractal Worlds* (Yale University Press, 2019).

12. M. Giona, First-order reaction—Diffusion kinetics in complex fractal media. *Chem. Eng. Sci.* **47**, 1503–1515 (1992).
13. R. Kopelman, Fractal reaction kinetics. *Science* **241**, 1620–1626 (1988).
14. Y. Gefen, A. Aharony, S. Alexander, Anomalous diffusion on percolating clusters. *Phys. Rev. Lett.* **50**, 77–80 (1983).
15. M.-O. Coppens, G. F. Froment, Diffusion and reaction in a fractal catalyst pore—I. Geometrical aspects. *Chem. Eng. Sci.* **50**, 1013–1026 (1995).
16. J. Crank, *The Mathematics of Diffusion* (Oxford University Press, Oxford, ed. 1, 1979).
17. S. Wang, Z.-F. Ma, H.-Q. Yao, Fractal diffusion model used for diffusion in porous material within limited volume of stiff container. *Chem. Eng. Sci.* **64**, 1318–1325 (2009).
18. B. O'Shaughnessy, I. Procaccia, Analytical solutions for diffusion on fractal objects. *Phys. Rev. Lett.* **54**, 455–458 (1985).
19. F. Stallmach, C. Vogt, J. Kärger, K. Helbig, F. Jacobs, Fractal geometry of surface areas of sand grains probed by pulsed field gradient NMR. *Phys. Rev. Lett.* **88**, 105505 (2002).
20. C. Bousige, P. Levitz, B. Coasne, Bridging scales in disordered porous media by mapping molecular dynamics onto intermittent Brownian motion. *Nat. Commun.* **12**, 1043 (2021).
21. J. Ślęzak, R. Metzler, Minimal model of diffusion with time changing Hurst exponent. *J. Phys. A Math. Theor.* **56**, 35LT01 (2023).
22. M. Niknam, L.-S. Bouchard, Nuclear induction lineshape: Non-Markovian diffusion with boundaries. *J. Chem. Phys.* **160**, 024305 (2024).
23. J. Stepišnik, P. T. Callaghan, The long time tail of molecular velocity correlation in a confined fluid: Observation by modulated gradient spin-echo NMR. *Phys. B Condens. Matter* **292**, 296–301 (2000).
24. G. E. Uhlenbeck, L. S. Ornstein, On the theory of the Brownian motion. *Phys. Rev.* **36**, 823–841 (1930).
25. U. Balucani, J. P. Brodholt, R. Vallauri, Analysis of the velocity autocorrelation function of water. *J. Phys. Condens. Matter* **8**, 6139–6144 (1996).
26. J. Stepišnik, C. Mattea, S. Stapf, A. Mohorič, Molecular velocity auto-correlation of simple liquids observed by NMR MGSE method. *Eur. Phys. J. B.* **91**, 293 (2018).
27. P. T. Callaghan, *Translational Dynamics and Magnetic Resonance* (Oxford University Press, 2011).
28. D. A. McQuarrie, *Statistical Mechanics* (University Science Books, Sausalito, ed. 1, 2000).
29. P. T. Callaghan, J. Stepišnik, Frequency-domain analysis of spin motion using modulated-gradient NMR. *J. Magn. Reson.* **117**, 118–122 (1995).
30. N. Leartprapun, Z. Zeng, Z. Hajjarian, V. Bossuyt, S. K. Nadkarni, Laser speckle rheological microscopy reveals wideband viscoelastic spectra of biological tissues. *Sci. Adv.* **10**, eadl1586 (2024).
31. M. Hua, Z. Peng, R. D. Guha, X. Ruan, K. C. Ng, J. Demarteau, S. Haber, S. Fricke, J. A. Reimer, M. B. Salmeron, K. A. Persson, C. Wang, B. A. Helms, Mechanochemically accelerated deconstruction of chemically recyclable plastics. *Sci. Adv.* **10**, eadq3801 (2024).
32. C. D. Sfatos, A. M. Gutin, E. I. Shakhnovich, Phase diagram of random copolymers. *Phys. Rev. E* **48**, 465–475 (1993).
33. F. Vaca Chávez, K. Saalwächter, Time-domain NMR observation of entangled polymer dynamics: Universal behavior of flexible homopolymers and applicability of the tube model. *Macromolecules* **44**, 1549–1559 (2011).
34. P. T. Callaghan, A. Coy, Evidence for reptational motion and the entanglement tube in semidilute polymer solutions. *Phys. Rev. Lett.* **68**, 3176–3179 (1992).
35. J. Tóth, A. L. Nagy, D. Papp, *Reaction Kinetics: Exercises, Programs and Theorems* (Springer New York, New York, NY, 2018).
36. S. N. Fricke, S. Haber, M. Hua, M. Salgado, B. A. Helms, J. A. Reimer, Magnetic resonance insights into the heterogeneous, fractal-like kinetics of chemically recyclable polymers. *Sci. Adv.* **10**, eadl0568 (2024).
37. T. X. Cai, N. H. Williamson, R. Ravin, P. J. Basser, Disentangling the effects of restriction and exchange with diffusion exchange spectroscopy. *Front. Phys.* **10**, 805793 (2022).
38. K. Kulasinski, R. Guyer, D. Derome, J. Carmeliet, Water diffusion in amorphous hydrophilic systems: A stop and go process. *Langmuir* **31**, 10843–10849 (2015).
39. D. Eager, A.-M. Pendrill, N. Reistad, Beyond velocity and acceleration: Jerk, snap and higher derivatives. *Eur. J. Phys.* **37**, 065008 (2016).
40. M. Visser, Jerk, snap and the cosmological equation of state. *Class. Quantum Gravity* **21**, 2603–2615 (2004).
41. M. S. Green, Markoff random processes and the statistical mechanics of time-dependent phenomena. II. Irreversible processes in fluids. *J. Chem. Phys.* **22**, 398–413 (1954).
42. T. X. Cai, N. H. Williamson, R. Ravin, P. J. Basser, The diffusion exchange ratio (DEXR): A minimal sampling of diffusion exchange spectroscopy to probe exchange, restriction, and time-dependence. *J. Magn. Reson.* **366**, 107745 (2024).
43. T. X. Cai, N. H. Williamson, V. J. Witherspoon, R. Ravin, P. J. Basser, A single-shot measurement of time-dependent diffusion over sub-millisecond timescales using static field gradient NMR. *J. Chem. Phys.* **154**, 111105 (2021).
44. D. Sinnaeve, The Stejskal–Tanner equation generalized for any gradient shape—an overview of most pulse sequences measuring free diffusion. *Concepts Magn. Reson. Part A* **40**, 39–65 (2012).
45. E. O. Stejskal, J. E. Tanner, Spin diffusion measurements: Spin echoes in the presence of a time-dependent field gradient. *J. Chem. Phys.* **42**, 288–292 (1965).
46. R. Mills, Self-diffusion in normal and heavy water in the range 1–45.deg. *J. Chem. Phys.* **77**, 685–688 (1973).
47. S. Yashonath, C. N. R. Rao, Structure and dynamics of polar liquids: A molecular dynamics investigation of N,N-dimethyl formamide. *Chem. Phys.* **155**, 351–356 (1991).
48. J. Geweke, S. Porter-Hudak, The estimation and application of long memory time series models. *J. Time Ser. Anal.* **4**, 221–238 (1983).
49. M. Schachter, M. D. Does, A. W. Anderson, J. C. Gore, Measurements of restricted diffusion using an oscillating gradient spin-echo sequence. *J. Magn. Reson.* **147**, 232–237 (2000).
50. M. P. Hollewand, L. F. Gladden, Transport heterogeneity in porous pellets—I. PGSE NMR studies. *Chem. Eng. Sci.* **50**, 309–326 (1995).
51. W. R. Alesi Jr., J. R. Kitchin, Evaluation of a primary amine-functionalized ion-exchange resin for CO_2 capture. *Ind. Eng. Chem. Res.* **51**, 6907–6915 (2012).
52. J. Fu, H. R. Thomas, C. Li, Tortuosity of porous media: Image analysis and physical simulation. *Earth Sci. Rev.* **212**, 103439 (2021).
53. W. E. Hart, M. Goldbaum, B. Côté, P. Kube, M. R. Nelson, Measurement and classification of retinal vascular tortuosity. *Int. J. Med. Inform.* **53**, 239–252 (1999).
54. M. Mächler, Very smooth nonparametric curve estimation by penalizing change of curvature (Technical Report, 1993), Vol. 71; https://doi.org/10.3929/ethz-a-000891329.
55. C. J. Gommes, A.-J. Bons, S. Blacher, J. H. Dunsmuir, A. H. Tsou, Practical methods for measuring the tortuosity of porous materials from binary or gray-tone tomographic reconstructions. *AIChE J.* **55**, 2000–2012 (2009).
56. I. R. Caldwell, V. O. Nams, A compass without a map: Tortuosity and orientation of eastern painted turtles (*Chrysemys picta picta*) released in unfamiliar territory. *Can. J. Zool.* **84**, 1129–1137 (2006).
57. S. Benhamou, How to reliably estimate the tortuosity of an animal's path:: straightness, sinuosity, or fractal dimension? *J. Theor. Biol.* **229**, 209–220 (2004).
58. E. Grisan, M. Foracchia, A. Ruggeri, A novel method for the automatic evaluation of retinal vessel tortuosity, in *Proceedings of the 25th Annual International Conference of the IEEE Engineering in Medicine and Biology Society (IEEE Cat. No.03CH37439)* (IEEE, 2003), pp. 866–869.
59. J. F. Douglas, F. Horkay, Influence of solvent quality on the swelling and shear modulus of polymer gels chemically cross-linked in solution. *MRS Adv.* **9**, 483–488 (2024).
60. A. Chremos, J. F. Douglas, P. J. Basser, F. Horkay, Molecular dynamics study of the swelling and osmotic properties of compact nanogel particles. *Soft Matter* **18**, 6278–6290 (2022).
61. J.-D. Bao, Time-dependent fractional diffusion and friction functions for anomalous diffusion. *Front. Phys.* **9**, 567161 (2021).
62. G. Parisi, N. Sourlas, Critical behavior of branched polymers and the Lee-Yang edge singularity. *Phys. Rev. Lett.* **46**, 871–874 (1981).
63. M. Becher, F. M. Salamanca, J. L. Valentin, K. Saalwächter, E. A. Rössler, Manifestation of Rouse and entanglement dynamics in non-cross-linked and cross-linked polymers studied by field-cycling and multiple quantum NMR. *J. Phys. Chem. B* **129**, 1082–1094 (2025).
64. M. Kale, F. Butar Butar, Fractal analysis of time series and distribution properties of Hurst exponent. *J. Math. Sci. Math. Educ.* **5**, 8–19 (2011).
65. S. Haber, J. Im, M. Hua, A. R. Epstein, S. N. Fricke, R. Giovine, H. Celik, K. A. Persson, B. A. Helms, J. A. Reimer, Mechanisms underpinning heterogeneous deconstruction of circular polymers: Insight from magnetic resonance methodologies. *Macromolecules* **58**, 1279–1288 (2025).
66. S. V. Kalinin, D. L. Gorbachev, A. Y. Borisevich, K. V. Tomashevitch, A. A. Vertegel, A. J. Markworth, Y. D. Tretyakov, Evolution of fractal particles in systems with conserved order parameter. *Phys. Rev. E* **61**, 1189–1194 (2000).
67. E. Salje, Kinetic rate laws as derived from order parameter theory I: Theoretical concepts. *Phys. Chem. Miner.* **15**, 336–348 (1988).
68. S. V. Kalinin, D. L. Gorbachev, K. V. Tomashevitch, A. Y. Borisevich, A. A. Vertegel, A. J. Markworth, Y. D. Tretyakov, Evolution of fractal particles in systems with conserved order parameter. *MRS Proceedings* **538**, 151–156 (1998).
69. M. McCormick, J. A. Reimer, NMR studies of structural phase transitions in random copolymers. *Macromolecules* **36**, 477–485 (2003).
70. J. Stepišnik, S. Lasič, A. Mohorič, I. Serša, A. Sepe, Velocity autocorrelation spectra of fluid in porous media measured by the CPMG sequence and constant magnetic field gradient. *Magn. Reson. Imaging* **25**, 517–520 (2007).
71. J. Stepišnik, I. Ardelean, A. Mohorič, Molecular self-diffusion in internal magnetic fields of porous medium investigated by NMR MGSE method. *J. Magn. Reson.* **328**, 106981 (2021).
72. G. Eidmann, R. Savelsberg, P. Blümler, B. Blümich, The NMR MOUSE, a mobile universal surface explorer. *J. Magn. Reson. A* **122**, 104–109 (1996).
73. B. Blümich, J. Anders, When the MOUSE leaves the house. *Magn. Reson.* **2**, 149–160 (2021).
74. H. Y. Carr, E. M. Purcell, Effects of diffusion on free precession in nuclear magnetic resonance experiments. *Phys. Rev.* **94**, 630–638 (1954).

75. S. Meiboom, D. Gill, Modified spin-echo method for measuring nuclear relaxation times. *Rev. Sci. Instrum.* **29**, 688–691 (1958).
76. B. Blümich, *NMR Imaging of Materials* (Clarendon Press, 2003).
77. J. Stepišnik, Validity limits of Gaussian approximation in cumulant expansion for diffusion attenuation of spin echo. *Phys. B Condens. Matter* **270**, 110–117 (1999).
78. J. Stepišnik, C. Mattea, S. Stapf, A. Mohorič, Molecular velocity auto-correlations in glycerol/water mixtures studied by NMR MGSE method. *Physica A: Stat. Mech. Appl.* **553**, 124171 (2020).

Acknowledgments: We acknowledge insightful conversations with M. Augustine, M. McCarthy, B. Blümich, and V. Witherspoon, as well as the use of imaging equipment from D. Bouchard of Alegre Science. **Funding:** This work was funded by the U.S. Department of Energy (DOE), Office of Science, Office of Basic Energy Sciences, Materials Sciences and Engineering Division under contract no. DE-AC02-05-CH11231 Unlocking Chemical Circularity in Recycling by Controlling Polymer Reactivity Across Scales program CUP-LBL-Helms. Work at the Molecular Foundry, including PDK synthesis, characterization, and acidolysis, was supported by the Office of Science, Office of Basic Energy Sciences, of the U.S. Department of Energy under contract no. DE-AC02-05CH11231. S.N.F. and A.-Y.S. acknowledge support as Pines Magnetic Resonance Center Postdoctoral Fellows. **Author contributions:** The CRediT author contributions are as follows: Conceptualization: S.N.F., M.S., J.A.R., B.A.H., M.H., and J.D. Methodology: S.N.F., J.A.R., and M.S. Investigation: S.N.F., M.S., J.D., A.-Y.S., M.H., and S.H. Visualization: S.N.F., S.H., and M.H. Supervision: J.A.R. and B.A.H. Writing–original draft: S.N.F. Writing–review & editing: S.N.F., S.H., J.D., A.-Y.S., J.A.R., and B.A.H. **Competing interests:** The authors declare the following competing interests: B.A.H. is an inventor on the US provisional patent application 62/587,148 submitted by Lawrence Berkeley National Laboratory that covers PDKs, as well as aspects of their use and recovery. B.A.H. and J.D. are inventors on the US provisional patent application 63/390,962 submitted by Lawrence Berkeley National Laboratory that covers biorenewable PDKs, as well as aspects of their use and recovery. B.A.H. has a financial interest in Cyklos Materials and Sepion Technologies. The other authors declare that they have no competing interests. **Data and materials availability:** The data that support the findings of this study are available from Dryad (https://doi.org/10.5061/dryad.80gb5mm13). The PDK materials used in this study can be provided by B.A.H. pending scientific review and a completed material transfer agreement. Requests for the PDK materials should be submitted to: foundry.lbl.gov. All other data needed to evaluate the conclusions in this paper are present in the paper and/or the Supplementary Materials.

Submitted 4 October 2024
Accepted 7 March 2025
Published 11 April 2025
10.1126/sciadv.adt6144